JPE 15-2-23

http://dx.doi.org/10.6113/JPE.2015.15.2.530
ISSN(Print): 1598-2092 / ISSN(Online): 2093-4718

Loss Analysis and Air-Cooled Design for a Cascaded Electrical Source Transmitter

Kai-chang Xue*, Shuang Wang*, Jun Lin†, Gang Li*, and Feng-dao Zhou*

*†College of Instrumentation and Electrical Engineering, Jilin University, Changchun, China

Abstract

Air-cooling method is adopted on the basis of the requirements for the thermal stability and convenient field use of an electrical source transmitter. The power losses of the transmitter are determined after calculating the losses of the alternating current (AC)–direct current (DC) power supply, the constant-current circuit, and the output circuit. According to the analysis of the characteristics of a heat sink with striped fins and a fan, the engineering calculation expression of the Nusselt number and the design process for air-cooled dissipation are proposed. Experimental results verify that the error between calculated and measured values of the transmitter losses is 12.2%, which meets the error design requirements of less than 25%. Steady-state average temperature rise of the heat sink of the AC–DC power supply is 22 °C, which meets the design requirements of a temperature rise between 20 °C and 40 °C. The transmitter has favorable thermal stability with 40 kW output power.

Key words: Air-cooled, Electrical source transmitter, Electromagnetic prospecting, Loss analysis

NOMENCLATURE

A_i	Area of baseplate outside, m^2
A_o	Total surface area of fins, m^2
c_a	Specific heat capacity of air, J/(kg°C)
c_l	Stripe coefficient
C	Perimeter of one fin, m
d	Hydraulic diameter of fin, m
E_{off}	Turn-off energy loss per pulse, J
E_{on}	Turn-on energy loss per pulse, J
E_{rr}	Reverse recovery energy loss per pulse, J
f	Friction factor
f_{app}	Apparent friction factor
h	Heat transfer coefficient, W/(m^2·°C)
H	Height of fin, m
k_a	Thermal conductivity of air, W/(m·°C)
k_f	Thermal conductivity of heat sink, W/(m·°C)
L	Heat sink length, m
L_s	Heat source length, m
n	Rotational speed of fan, r/min
n_f	Fin number of heat sink
n_m	Rate value of the rotational speed of fan, r/min
N	Shaft power of fan, W
N_m	Rate value of the shaft power of fan, W
Nu	Nusselt number, hs/k_a
NUT	Number of transfer units
p	Static pressure of fan, Pa
p_m	Rate value of the static pressure of fan, Pa
Pr	Prandtl number, ≈ 0.7 for air
ΔP_a	Total pressure drop, Pa
ΔP_l	Total pressure drop of inlet and outlet, Pa
ΔP_c	Core pressure drop, Pa
P	Power, W
P_{off}	Turn-off loss, W
P_{on}	Turn-on loss, W
P_{rr}	Reverse recovery loss, W
Q	Volumetric flow rate, m^3/min
Q_m	Rate value of the volumetric flow rate of fan, m^3/min
Q_{rr}	Reverse recovery charge of diode, C
R	Thermal resistance, °C /W
Re	Reynolds number, $V_a s/v$
s	Fin spacing, m
t_a	Fin thickness in root, m
t_b	Baseplate thickness, m
T	Temperature, °C
T_a	Air temperature, °C
T_f	Temperature of baseplate inside, °C

Manuscript received Jul. 18, 2014; accepted Oct. 13, 2014
Recommended for publication by Associate Editor Honnyong Cha.
†Corresponding Author: lin_jun@jlu.edu.cn
Tel: +86-130-1910-0118, Jilin University
*College of Instrumentation and Electrical Eng., Jilin University, China

V_a Average velocity in fin channel, m/s
V_{amax} Maximum velocity in fin channel, m/s
W Heat sink width, m
W_s Heat source width, m
Greek Symbols
ρ_a Air density, kg/m^3
ρ_P Intensity of internal thermal source, W/m^3
η Efficiency of transmitter
η_f Fin efficiency
η_a Air viscosity under inlet and outlet average air temperature, P$_a$·s
η_a Air viscosity under fin surface temperature, Pa·s
ε Contraction ratio
v Kinematic viscosity, m^2/s

I. INTRODUCTION

Electromagnetic prospecting methods directly obtain underground information by using electromagnetic theory, which is widely used in water, mineral, and hydrocarbon resource explorations, as well as in other fields [1]-[3]. In controlled source audio-frequency magnetotelluric method, direct current resistivity method, and induced polarization method, the electrical source transmitter is the artificial excitation source for electromagnetic prospecting. The load of the electrical source transmitter is two electrode holes away from each other for 1–3 km on the ground, with an equivalent resistance of approximately 10–80 Ω. The transmitter must provide an exciting current to the earth load in practical applications, and the exciting current is approximately 10–40 A. Maximum output voltage usually needs to reach 1000 V, and transmitter power usually needs to reach tens of kW. For transmitters with a power of tens of kW, thermal losses can reach several kW.

Several transmitters have been developed in the field of geophysical instruments [4]-[8]. A transmitter developed by the Central South University of China and used for wide-area electromagnetic sounding has 200 kW output power [5]. The Institute of Geophysical and Geochemical Exploration under the Chinese Academy of Geological Sciences developed the DEM-T70 transmitter, which has 70 kW output power [7], [8]. An American company, Zonge International, developed the GGT-30 transmitter, which has 30 kW output power. These power devices of transmitters, used to acquire direct current (DC) bus voltage, work below 400 Hz. These transmitters have high efficiency and output power. However, the system response speed is low, and the effect of suppressing transient earth load fluctuation should be improved. Therefore, these transmitters achieve high thermal stability at the cost of control precision. The Canadian Phoenix Company developed the TXU-30 transmitter. The power devices of TXU-30 work at 20 kHz, which has high control precision. However, China is the main area where electrical source transmitters are used, and TXU-30 uses a three-phase 220 V generator instead of the three-phase 380 V mainstream generator used in China. Therefore, the thermal design of TXU-30 is not suitable for transmitters with 380 V input. In addition, the power of TXU-30 is 20 kW, and its thermal losses are relatively low.

In the field of power electronics, research is focused on the loss calculation of power devices, whereas thermal dissipation analysis is comparatively scarce. The analysis method of thermal dissipation proposed in Ref. [9] involves several coefficients, but Ref. [9] does not show how to determine the coefficients, which limits its use for engineering applications. Ref. [10] disregards the effect of the efficiency of heat sink fin, and the thermal dissipation analysis is relatively rough. In Refs. [11]-[17], the analysis of heat sink is comprehensive, and several calculation expressions are introduced. However, the expressions proposed in these studies are generally complex, adding to the complexity of the engineering design. These studies also focus on a heat sink with smooth fins rather than the widely used one with striped fins. In the heat transfer field [18], thermal dissipation theories are systematically illustrated. However, these theories are generally macroscopic, and few studies show the corresponding analysis of air-cooled design on the basis of power circuit.

A heat sink with striped fins is analyzed in the present study on the basis of the characteristics of an electrical source transmitter, the classical theory of heat transfer, and the research results for heat sinks. Fan characteristics are studied based on the research results for hydromechanics. An engineering design process for air-cooled thermal dissipation is proposed. Experimental results verify that the transmitter has favorable thermal stability when the outputs are 1000 V and 40 A. The calculation error of thermal losses of the transmitter and the temperature rise of the heat sink are reasonable. The proposed air-cooled method can be applied to other power electronic equipment below 100 kW to a certain extent.

This paper includes several symbols that are not easy to remember. Hence, the definitions of the main symbols are listed after the Abstract.

II. DESIGN PURPOSES

The main purpose of the thermal design is to ensure the safety of devices in the transmitter, especially the security of power semiconductor devices. When the main purpose is met, another secondary purpose of the thermal design is considered. The secondary purpose is to ensure that the size and weight of the heat sink are as small as possible, making it convenient for field application.

For power semiconductor devices, the maximum allowable junction temperature of the tube core is generally 125 °C –150 °C. The maximum junction temperature T_{jmax} can be obtained from device specifications, and the junction temperature is represented as T_j or T_{vj} in device specifications.

TABLE I
FAN PARAMETERS OF DELTA COMPANY

Size (cm)	N_m (W)	Q_m (m^3/min)	p_m (Pa)
12 × 12 × 3.8	1.7–48	2.02–7.16	41.4–352
9.2 × 9.2 × 3.8	4.0–37	1.93–4.95	76.0–453
8 × 8 × 3.8	2.4–18	1.28–2.89	69.9–307
6 × 6 × 2.54	0.84–9.0	0.541–1.45	32.0–253

The temperature loss, ΔT_1, between the tube core and the case of the device is 10 °C–25 °C. $\Delta T_1 = P \cdot R_{thJC}$, where P represents the power loss of the device, and R_{thJC} represents the thermal resistance between the tube core and the case. R_{thJC} can be obtained from device specifications, and some specifications also adopt $R_{th(j-c)}$. Insulation pad, contact gap, and so on will induce a loss, ΔT_2, of 10 °C–25 °C between the device and the heat sink. For power modules, the case is generally insulated against device pins. $\Delta T_2 = P \cdot R_{thCK}$, where R_{thCH} represents the contact thermal resistance between the case and the heat sink. R_{thCK} can be obtained from device specifications, and some specifications also adopt $R_{th(c-k)}$. For discrete power devices, the case is generally connected to one pin of a device. Thus, an insulation pad should be added between the case and the heat sink. $\Delta T_2 = P \cdot (R_{thCK} + R_{ic})$, where R_{ic} represents the thermal resistance of the insulation pad. The calculation of R_{ic} will be shown in Section IV.A. The local temperature of the heat sink where the power device is located is higher than the average temperature of the heat sink, and the temperature loss ΔT_3 is approximately 10 °C. $\Delta T_3 = P \cdot R_{cb}$. The calculation of R_{cb} will be shown in Section IV.A, which is from Ref. [17]. The maximum temperature T_{amax} in the field in summer may be 35 °C–38 °C. Therefore, the average temperature rise ΔT_{hs} of the heat sink should be less than 40 °C, where $\Delta T_{hs} = T_{jmax} - \Delta T_1 - \Delta T_2 - \Delta T_3 - T_{amax}$. Although a low temperature rise will increase the reliability of the devices, it will also increase the size and weight of the heat sink. A significantly low temperature rise does more harm than good. Therefore, the temperature rise should be kept between 20 °C and 40 °C.

To control the temperature rise of the heat sink, the device losses should be calculated. When loss error is too high, the selected heat sink will be obviously small or large. The small size of the heat sink will cause a high temperature rise, which endangers the safety of the devices. The large size of the heat sink will cause the transmitter to become very heavy. Given that the power dissipation of the heat sink is approximately proportional to the size and weight of the heat sink with the same structure and with the size difference below several tens of percent (Figs. 2(d) and 5(a) in Ref. [19]), the loss error between 0% and +25% does not significantly increase the transmitter weight. Volumetric flow rate Q_m and static pressure p_m are also different for same-sized fans, as shown in Table I [20]. $Q \propto P/\Delta T_a$, where P represents the power loss, Q represents the volumetric flow rate of the fan, and ΔT_a represents the temperature difference between inlet and outlet air. The error can be feasibly and easily compensated by replacing the fan with the same size when the loss error is between 0% and −25%. A low loss error needs a highly accurate mathematical model and must consider numerous factors [21]-[23]. Some stray losses are difficult to calculate, and the actual conditions are not exactly the same as the testing conditions in the specification. These conditions include voltage [21], current [21], junction temperature [21], device driver [22], pulse width [23], and circuit topologies. Therefore, selecting 25% as the accepted loss error is a relatively reasonable trade-off between application value and calculation complexity.

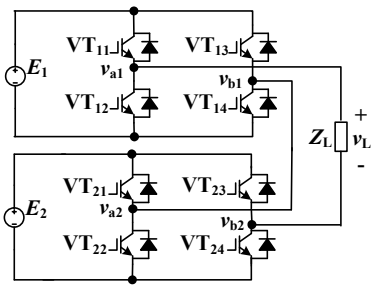

Fig. 1. Principle of the cascaded topology.

TABLE II
SWITCHING LOSSES OF DIFFERENT IGBTS

Loss categories	600 V		1200 V		3300 V	
	Q_{rate}	Q/kW	Q_{rate}	Q/kW	Q_{rate}	Q/kW
E_{on} (mJ)	1.6	0.05	9	0.15	170	0.94
E_{off} (mJ)	4.0	0.13	12	0.20	140	0.78
E_{rr} (mJ)	3.0	0.10	12.4	0.21	185	1.03

III. TRANSMITTER LOSSES

A. Cascaded Topology of the Transmitter

The transmitter adopts the cascaded topology shown in Fig. 1, where Z_L represents the earth load of the transmitter. When VT_{11}, VT_{14} and VT_{21}, VT_{24} turn on, the load voltage is $v_L = E_1 + E_2 = 2E$, and the output is a positive pulse. When VT_{12}, VT_{13} and VT_{22}, VT_{23} turn on, the load voltage is $v_L = -(E_1 + E_2) = -2E$, and the output is a negative pulse. The output level of the transmitter is only $+2E$ and $-2E$ without $+E$, $-E$, and 0, which is different from the conventional cascaded multilevel inverters [24]-[26]. E_1 and E_2 are in a floating state that refers to the load Z_L. Therefore, the rated voltage of the insulated gate bipolar transistors (IGBTs) can be half of the integrated transmitter, which can reduce the design difficulty and the switching losses of the transmitter.

Table II shows the relationship between maximum rated voltage and switching losses of different IGBTs. In Table II, the switching loss parameters of 600, 1200, and 3300 V IGBTs are from the IGBT modules marked FF200R06KE3, FF200R12KT4, and FF200R33KF2C, respectively. E_{on}, E_{off},

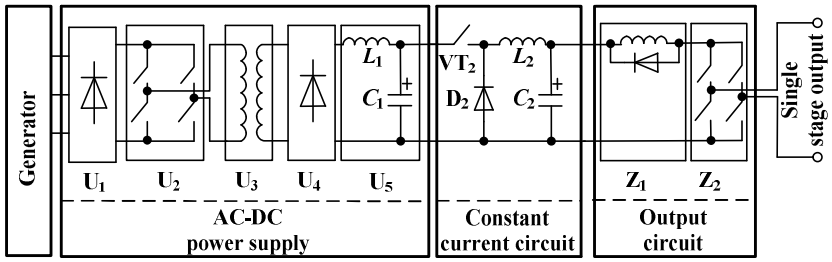

Fig. 2. Circuit diagram of a single-stage transmitter.

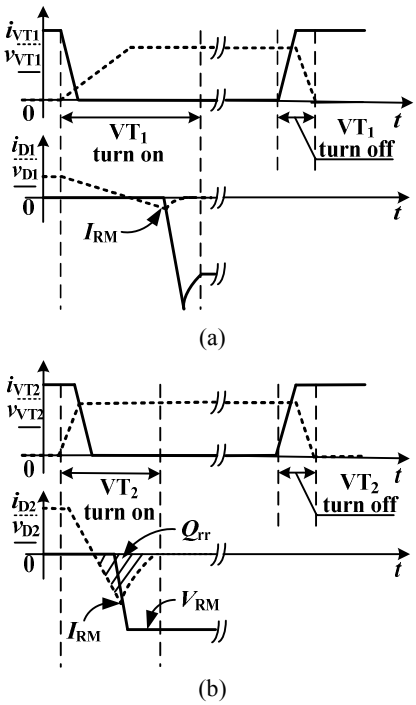

Fig. 3. Switching loss analysis. (a) AC–DC power supply. (b) The constant-current circuit.

and E_{rr} represent turn-on, turn-off, and diode reverse recovery energy losses per pulse, respectively. Q_{rate} is the energy losses under the rated power. For 600, 1200, and 3300 V IGBTs, the rated powers are 300 V/100 A, 600 V/100 A, and 1800 V/100 A, respectively. For comparison, the energy losses are normalized to per kW, which is represented as $Q_{/kW}$ in Table II. Table II shows that the switching losses of 600 V IGBT are approximately half of those of 1200 V IGBT. Meanwhile, the switching losses of 3300 V IGBT are approximately five times those of 1200 V IGBT. Therefore, cascaded topology can reduce switching losses.

The circuit of the single-stage transmitter involved in the cascaded technology is shown in Fig. 2. The AC–DC power supply converts the 380 V AC provided by the generator to 550 V DC, and the high-frequency transformer isolates the input and the output. The constant-current circuit makes the average current in the chopper inductance L_2 the set value by adjusting the chopper-circuit switch VT_2; that is, it maintains the output current of the chopper circuit at the set value. The output full-bridge Z_2 of the output circuit with another output full bridge in another single-stage transmitter comprises the cascaded topology shown in Fig. 1.

B. Single-Stage Transmitter Losses

Considering that the entire electrical source transmitter consists of two single-stage transmitters in series, only the thermal losses of the single-stage transmitter must be analyzed.

1) Switching Losses: When any IGBT of the four IGBTs involved in the full-bridge inverter U_2 is represented as VT_1, any diode of the high-frequency rectifier U_4 is represented as D_1, the chopper switch IGBT is represented as VT_2, and the chopper diode is represented as D_2. The voltage and current waveforms of IGBTs and diodes during the turn-on and turn-off are shown in Fig. 3. In Fig. 3, i_{VT1} and v_{VT1} represent the current and voltage of VT_1 when VT_1 turns on and turns off respectively. i_{D1} and v_{D1} represent the current and voltage of D_1 during the reverse recovery respectively. i_{VT2} and v_{VT2} represent the current and voltage of VT_2 when VT_2 turns on and turns off respectively. i_{D2} and v_{D2} represent the current and voltage of D_2 during the reverse recovery respectively.

In Fig. 3(a), the overlapping area between i_{VT1} and v_{VT1} is small when VT_1 turns on because the leakage inductance of the transformer suppresses the changing rate of the current. The slope of the diode current i_{D1} is relatively low when i_{D1} drops from the positive steady-state current I_F to the maximum reverse value $-I_{RM}$. The overlapping area between i_{D1} and v_{D1} is small. This situation is not in accordance with the test conditions for the turn-on loss of the IGBT in the specifications. Therefore, the turn-on loss of VT_1 and the reverse recovery loss of D_1 are lower than the turn-off energy loss E_{on} and the reverse recovery energy loss E_{rr} in the specification. When VT_1 turns off, no other circulation loop exists, except VT_1 for the current in the primary side of the transformer before the voltage v_{VT1} rises from 0 to bus voltage. Therefore, i_{VT1} remains the initial current value, and the overlapping area between i_{VT1} and v_{VT1} is large. The turn-off is in accordance with the test conditions in the specifications. Therefore, the turn-off energy loss E_{off} can be used to calculate the turn-off loss.

In Fig. 3(b), the overlapping area between i_{VT2} and v_{VT2} is large when VT_2 turns on because v_{VT2} is clamped to the input voltage before i_{VT2} rises from 0 to the steady-state value. The

TABLE III
AC–DC POWER SUPPLY LOSSES

Symbols	Losses (W)	Symbols	Losses (W)
P_{U1}	190	P_{L1}	50
P_{U2}	4 × 137	P_{U6}	110
P_{U2R}	4 × 7	P_{U7}	24 × 2
P_{U3}	72	P_{U8}	50
P_{U4}	8 × 52	P_{U9}	100
P_{U4R}	76		

changing rate that the current i_{D2} in diode D_2 decreases from the positive steady-state current I_F to 0 is determined by the inherent rate of the IGBT. The changing rate of the IGBT inherent current is fast when it turns on. Therefore, the peak value I_{RM} of the reverse recovery current of the diode D_2 is large. The overlapping area between i_{D2} and v_{D2} is also large. When VT_2 turns off, the current of chopper inductance L_2 can only flow through VT_2 before the voltage v_{VT2} increases from 0 to the input voltage. Therefore, the overlapping area between i_{VT2} and v_{VT2} is large. The turn-on and turn-off of VT_2 and the reverse recovery of the diode D_2 are in accordance with the specifications of IGBT test conditions. E_{on}, E_{off}, and E_{rr} can thus be used to calculate VT_2 and D_2 losses.

For the IGBTs involved in the output full-bridge Z_2 in the output circuit, the turn-off process is consistent with that of VT_1. The turn-off energy loss E_{off} can be used to calculate the turn-off loss. The turn-on process is also consistent with that of VT_1. However, the load inductance is larger than the leakage inductance of the transformer. Turn-on loss is lower than that of VT_1, which can thus be ignored.

Eq. (1) can be used to calculate the corresponding switching losses when the situation is equivalent to the test conditions in the specification. It is expressed as follows:

$$P_x = E_x \cdot f_S \cdot (V / V_{REF}) \cdot (I / I_{REF}), \quad (1)$$

where x can be on, off, or rr, which respectively represents the turn-on of the IGBT, turn-off of the IGBT, or reverse recovery of the diode. E_x represents the energy losses with the testing voltage V_{REF} and the testing current I_{REF} in the specification. V and I represent the actual working voltage and current of the power device respectively. P_x represents the power losses. f_s represents the switching frequency.

For some diodes, the specification does not give E_{rr}. Eq. (2) can be used to calculate E_{rr} of the diode, that is,

$$E_{rr} = V_{RM} Q_{rr} / 2, \quad (2)$$

where V_{RM} is the reverse steady-state voltage of the diode. Q_{rr} is the reverse recovery charge, which can be found in the specification.

2) Total Losses: The output of the AC–DC power supply is designed to be 550 V and 45 A, and the power is 25 kW. The 50 Hz rectifier U_1 of the AC–DC power supply adopts VUO110-16NO7, the input contactor adopts CJX2-6511, and the full-bridge inverter U_2 adopts the IGBT module FF200R12KT4, which operates in 18 kHz. The high-frequency rectifier U_4 adopts a full-bridge rectifier, and the single-bridge leg consists of four diodes in series, which adopt the diode module MEE250-012DA. The full-bridge inverter U_2 adopts the resistor–capacitor (RC) snubber circuit to eliminate resonance. Each IGBT parallels an RC snubber, with R of 100 Ω and C of 3.3 nF. The high-frequency transformer U_3 adopts 3 EE110 cores in parallel, 7 turns in primary, and 10 turns in secondary. Each turn in primary and secondary uses double Liz wires, Φ 0.1 mm × 800, in parallel. The high-frequency rectifier U_4 also adopts an RC snubber, with R of 50 Ω and C of 6.8 nF. The RC snubber parallels the secondary of the high-frequency transformer U_3, and the output inductance L_1 adopts four EE110 cores in parallel. The air gap is 12.8 mm, and the number of turns is 27. Each turn uses double Liz wires, Φ 0.1 mm × 800, in parallel. Table III shows the calculated value of the AC–DC power supply losses.

In Table III, P represents the losses, the subscript U_1 represents the 50 Hz rectifier, U_2 represents the full-bridge inverter, U_{2R} represents the snubber resistance of the full-bridge inverter U_2, U_3 represents the high-frequency transformer, U_4 represents the high-frequency rectifier, U_{4R} represents the RC snubber resistance of the high-frequency rectifier, L_1 represents the output inductor, U_6 represents the fan and its power supply, U_7 represents the resistance used to balance the voltage of the series capacitor C_1, U_8 represents the input contactor, and U_9 represents other stray losses. The losses of U_1, U_2, U_{2R}, U_4, and U_{4R} are 1258 W. These devices are fixed on a heat sink. The total losses of the AC–DC power supply are 1688 W. The efficiency of the AC–DC power supply is 93.2%.

The constant-current circuit output is designed to be 500 V and 50 A, and the power is 25 kW. The working frequency of the chopper circuit is 18 kHz. The chopper switch VT_2 and the chopper diode D_2 adopt the internal integration devices of the IGBT module FF200R12KT4. The constant-current inductance L_2 is in accordance with the output inductance L_1 of the AC–DC power supply. The diode of the short-circuit protection circuit Z_1 adopts MEK250-12DA, which has two parallel internal diodes. The inductance of the short-circuit protection circuit Z_1 adopts nine EE55 cores in parallel, the air gap is 2.25 mm, and the number of turns is 7.5. Each turn uses double Liz wires, Φ 0.1 mm × 800, in parallel. The full-bridge Z_2 adopts the IGBT module 2MBI200U4H-170. Each IGBT parallels an RC snubber, with R of 100 Ω and C of 3.3 nF. The working frequency is 1–10 kHz. Given that the load is inductive, the current generally cannot be more than 20 A when the transmitting frequency of the output full-bridge Z_2 is higher than 1 kHz. Therefore, 2 kHz and 20 A are adopted to calculate the losses of Z_1 and the output full-bridge Z_2. Table IV shows the calculated losses of the constant-current circuit and the output circuit.

In Table IV, P represents the losses, the subscript VT_2 represents the chopper switch, D_2 represents the chopper

TABLE IV
LOSSES OF CONSTANT-CURRENT CIRCUIT AND OUTPUT CIRCUIT

Symbols	Losses (W)	Symbols	Losses (W)
P_{VT2}	223	P_{Z2}	4 × 47
P_{D2}	132	P_{Z2R}	4 × 4
P_{L2}	50	P_{Z3}	24 × 2
P_{Z1D}	60	P_{Z4}	110
P_{Z1L}	17	P_{Z5}	100

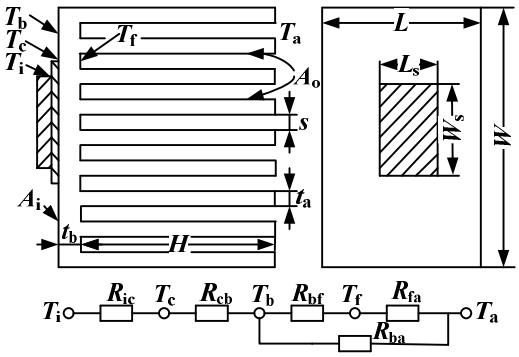

Fig. 4. Thermal resistance model.

diode, L_2 represents the inductance of the constant-current circuit, Z_{1D} represents the diode of the short-circuit protection circuit, Z_{1L} represents the short-circuit protection inductance, Z_2 represents the output full bridge, Z_{2R} represents the RC snubber of the full-bridge Z_2, Z_3 represents the resistance used to balance the voltage of series capacitor C_2, Z_4 represents the fan and its power supply, and Z_5 represents other stray losses. The total losses of the constant-current circuit and the output circuit are 944 W. The losses of VT_2, D_2, Z_{1D}, Z_{1L}, Z_2, and Z_{2R} are 619 W. These devices are fixed on a heat sink. Therefore, the comprehensive efficiency of the constant-current circuit and the output circuit is 96.2%.

The preceding analysis indicates that the design losses of the single-stage transmitter are 2632 W, and the efficiency is 89.5%.

IV. AIR-COOLED DESIGN

A. Thermal Resistance Model

Fig. 4 shows the thermal resistance model. The length and width of the heat source are L_s and W_s respectively. The heat source is attached to the heat sink with the insulation pad. The length and width of the heat sink are L and W respectively. The height of the fin and the thickness in the root are H and t_a respectively. The fin spacing is s. A_i is the area of the outside of the baseplate, and A_o is the total surface area of the fins. The thickness of the baseplate is t_b. The equivalent circuit of thermal resistance is shown at the bottom of Fig. 4. T_i, T_c, T_b, T_f, and T_a represent the temperature of the heat source, the baseplate side of the insulation pad, the outer surface of the baseplate, the inside of the baseplate, and the air, respectively. R_{ic}, R_{cb}, R_{bf}, R_{fa}, and R_{ba} represent the thermal resistance of the insulation pad, the insulation pad to the outer surface of the baseplate, the baseplate, the fins to the air, and the outer surface of the baseplate to the air [17].

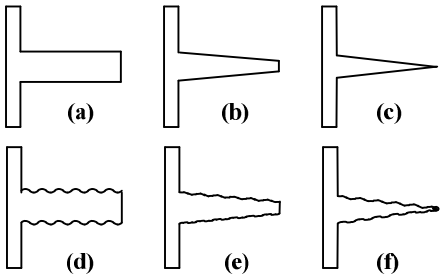

Fig. 5. Heat sink fins. (a) Straight fin. (b) Trapezoidal fin. (c) Triangular fin. (d) Straight fin with stripes. (e) Trapezoidal fin with stripes. (f) Triangular fin with stripes.

$$R_{ic} = t_c / \left(k_c L_s W_s\right), \tag{3}$$

where t_c and k_c represent the thickness and the thermal conductivity of the insulation pad respectively.

$$\begin{aligned} R_{cb} = {} & \frac{8}{L_s^2 L W k_f} \sum_{m=1}^{\infty} \frac{\sin^2\left(\delta_m L_s / 2\right)}{\delta_m^3} \phi\left(\delta_m\right) \\ & + \frac{8}{W_s^2 L W k_f} \sum_{n=1}^{\infty} \frac{\sin^2\left(\lambda_n W_s / 2\right)}{\lambda_n^3} \phi\left(\lambda_n\right) \\ & + \frac{16}{L_s^2 W_s^2 L W k_f} \sum_{m=1}^{\infty}\sum_{n=1}^{\infty} \frac{\sin^2\left(\delta_m L_s / 2\right)\sin^2\left(\lambda_n W_s / 2\right)}{\delta_m^2 \lambda_n^2 \beta_{m,n}} \phi\left(\beta_{m,n}\right) \end{aligned}, \tag{4}$$

where

$$\phi(\zeta) = \frac{\left(e^{2t_b\zeta}+1\right)\zeta - \left(1-e^{2t_b\zeta}\right)h_{eff}/k_f}{\left(e^{2t_b\zeta}-1\right)\zeta - \left(1+e^{2t_b\zeta}\right)h_{eff}/k_f},$$

$$h_{eff} = hA_o\eta_f / A_i,$$

h is the heat transfer coefficient of the heat sink to air. η_f is the efficiency of the heat sink, $\delta_m = 2m\pi/L$, $\lambda_m = 2n\pi/W$, $\beta_{m,n} = \left(\delta_m^2 + \lambda_n^2\right)^{1/2}$, and k_f is the thermal conductivity of the heat sink.

$$R_{bf} = t_b / \left(k_f A_i\right) \tag{5}$$

$$R_{ba} = 1 / \left(hA_i\right) \tag{6}$$

$$R_{fa} = 1 / \left(hA_o\eta_f\right) \tag{7}$$

B. Efficiency of Striped Fins

The shapes of common heat sink fins, including rectangular, trapezoidal, and triangular fins, are shown in Fig. 5. Stripes are usually engraved on fins to increase the surface area of thermal dissipation in engineering applications. Refs. [11]-[18] provided some calculation methods for smooth fins. However, few reports have discussed the effect of striped fins. The efficiency of striped fins will be analyzed in the following section on the basis of the known analysis of smooth fin.

For the heat sink of thermal dissipation power above 100 W, air velocity V_a in the fin channel is lower than 5 m/s,

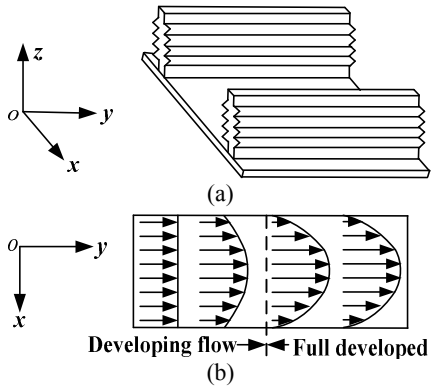

Fig. 6. Laminar flow in striped fin channel.

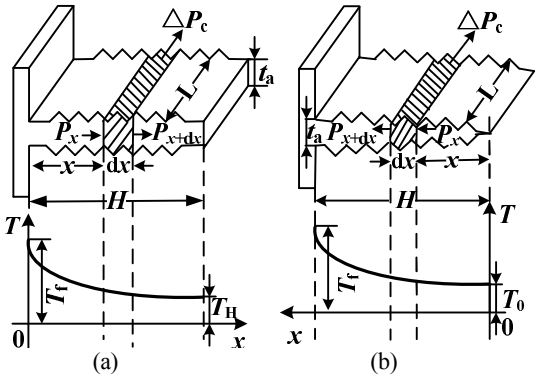

Fig. 7. Analysis diagram of the efficiency of striped fins. (a) Straight fin analysis. (b) Triangular fin analysis.

and fin spacing s is lower than 7×10^{-3} m in general. Air kinematic viscosity v is approximately 17×10^{-6} m^2/s and around 40 °C. Therefore, Reynolds number $Re = V_a \cdot s/v < 2200$, and the air flow in the fin channel is laminar flow [18]. Fig. 6 shows the laminar flow in the striped fin channel. When the air flows in the fin channel along y direction, given that the direction of the stripe groove coincides with the direction of the air flow, the striped fin cannot change the air flow direction. The air only flows in the xOy plane, as shown in Fig. 6(b). The air velocity is uniform at x direction in inlet. When air from the developing flow section enters the fully developed section, the air velocity is larger in the middle and lower in both sides. The nature of air flow in striped fins and smooth fins is the same.

The main difference between striped and smooth fins is the surface area of the fins. The stripe coefficient c_1 in Eq. (8) can be used to express the difference, that is,

$$c_1 = A_o / (2n_f LH), \tag{8}$$

where A_o represents the total surface area of the fins, and n_f represents the fin number of the heat sink.

Fig. 7 shows the 1D analysis model of the efficiency of striped fins. According to the thermal conduction differential equation,

$$\frac{d}{dx}\left[A_f(x)\frac{dT}{dx}\right] + \frac{\rho_P}{k_f} = 0, \tag{9}$$

where T is the temperature variable, and ρ_p is the intensity of the internal thermal source. $A_f(x)$ represents the cross-sectional area of the fin along the x direction. $A_f(x) = t_a L$ for straight fin, and $A_f(x) = t_a Lx/H$ for triangular fin. The boundary conditions for straight fin are $x = 0$, $T = T_f$ and $x = H$, $dT/dx = 0$. The boundary conditions for straight fin are $x = 0$, $T \neq \infty$ and $x = H$, $T = T_f$. According to Fig. 7, the thermal power losses on dx are as follows:

$$\begin{aligned}\Delta P_c &= |P_x - P_{x+dx}| = \rho_p L t_a(x)dx \\ &= hc_1 C(T - T_a)dx \approx 2hc_1 L(T - T_a)dx\end{aligned}, \tag{10}$$

where C is the perimeter of the fin, which approximately equals $2L$; $t_a(x)$ is the function of the fin thickness along x direction; $t_a(x) = t_a$ for straight fin; and $t_a(x) = t_a x/H$ for triangular fin. According to Eq. (10),

$$\rho_p = 2hc_1(T - T_a)/t_a(x). \tag{11}$$

The function of the fin temperature T along the x direction can be obtained by uniting Eq. (9), Eq. (11), and $t_a(x)$, and it will be denoted by $T(x)$. According to $T(x)$ and the expression of the Fourier's law shown in Eq. (12), the efficiency expressions of the rectangular striped fin and the triangular striped fin can be obtained, as shown respectively in Eqs. (12) and (13).

$$P = -k_f L t_a(x) \cdot dT/dx \tag{12}$$

$$\eta_f = \frac{P}{P_0} = \frac{\text{th}(\sqrt{2}\sqrt{hc_1/(k_f A_V)}H^{3/2})}{\sqrt{2}\sqrt{hc_1/(k_f A_V)}H^{3/2}}, \quad A_V = t_a H \tag{13}$$

$$\eta_f = \frac{P}{P_0} = \frac{I_1(2\sqrt{hc_1/(k_f A_V)}H^{3/2})}{I_0(2\sqrt{hc_1/(k_f A_V)}H^{3/2})}, \quad A_V = t_a H/2 \tag{14}$$

In Eqs. (13) and (14), P represents the actual thermal dissipation of the fin, and P_o represents the thermal dissipation when the fin keeps the temperature in the root from the root to the terminal. I_1 and I_0 represent the 1-order and 0-order first-kind-modified Bessel functions respectively.

According to Eqs. (13) and (14), the efficiency curves of the striped fins shown in Fig. 8 can be obtained. Therefore, the efficiencies of the striped rectangular striped fin and the triangular striped fin can be obtained by evaluating the efficiency curves shown in Fig. 8. Calculating accurate results for the striped trapezoidal fin is difficult. The efficiency can be replaced by the average value of the triangular striped fin efficiency and the rectangular striped fin efficiency when $A_V = (t_a + t_m)H/2$ is used. t_m represents the thickness of the terminal of the trapezoidal fin. When $c_1 = 1$, Eq. (13), Eq. (14), and Fig. 8 can also be used to calculate the efficiencies of smooth fins.

C. Heat Transfer Coefficient

Heat transfer coefficient h is the key parameter in calculating Eqs. (4), (6), and (7), as well as the function of the Nusselt

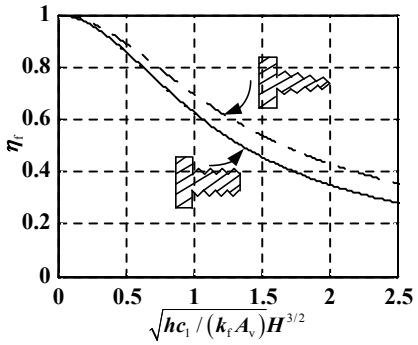

Fig. 8. Efficiency curves of striped fins.

number, *Nu*. Unless otherwise stated, $h = Nuk_a/s$ is considered in the following sections, and k_a is the air thermal conductivity. This section focuses on the calculation of *Nu*.

Air flows in the heat sink. Air flow can be divided into developing flow, transition, and fully developed sections. Except for special specifications in the following sections, $Re = V_a s/\nu$, where V_a is the air velocity, and ν is the kinematic viscosity. Before analysis, $x^+ = Re \cdot s/L$ and $x^* = Re \cdot \Pr \cdot s/L$ are defined, where *Pr* is the Prandtl number, and *Pr* is approximately equal to 0.7 for air.

1) Developing Flow Section: For the developing flow section, Refs. [11] and [12] adopted the expression shown in Eq. (15), Ref. [13] adopted the expression shown in Eq. (16), Ref. [18] adopted the expression shown in Eq. (17), and Refs. [14] and [15] adopted the expressions shown in Eq. (18).

$$Nu = 0.664\sqrt{x^+}\,\Pr^{1/3}\left(1+3.65\Big/\sqrt{x^+}\right)^{1/2} \tag{15}$$

$$Nu = 2Nu',\quad Nu' = 1.89 + \frac{0.142\Pr^{1/3}\left(0.25x^+\right)^{1.14}}{1+0.211\left(0.25x^+\right)^{0.64}} \tag{16}$$

$$Nu = 1.86\left(Re\Pr d/L\right)^{1/3}\cdot\left(\eta_a/\eta_h\right)^{0.14},\quad Re\Pr d/L > 10 \tag{17}$$

$$\begin{cases} h = \dfrac{m_a c_a}{A_a}\left(1-e^{-NTU}\right),\ m_a = \rho_a V_{amax} WH, \\ NTU = h_{LMTD}\dfrac{A_a}{m_a c_a},\ h_{LMTD} = \dfrac{Nu_{LMTD}' k_a}{2s} \\ Nu_{LMTD}' = 7.43237 + 0.0405984\cdot 4x^* - 1.17060\cdot 10^{-4}\cdot\left(4x^*\right)^2 \\ \qquad + 2.42627\cdot 10^{-7}\cdot\left(4x^*\right)^3 - 13.1211\left(s/H\right) \\ 0 < \dfrac{s}{H} < \dfrac{1}{6} \end{cases} \tag{18a}$$

When only one channel of fins is analyzed, Eq. (18a) can be simplified as follows:

$$Nu = 2x^*\left(1-e^{-Nu_{LMTD}'/x^*}\right). \tag{18b}$$

In Eqs. (15)–(18), *d* is the equivalent hydraulic diameter of the conduit, *NTU* is the number of transfer units, and A_a is the total surface area of the heat sink. η_a is the viscosity of the air under the inlet and the outlet average air temperatures, and η_h is the viscosity of air under the fin surface temperature. This study considers that $\eta_a = \eta_h$. ρ_a is the air density. V_{amax} is the maximum velocity of the air flow between fins, and is approximately twice the average velocity of V_a.

2) Fully Developed Section: For the fully developed section, Ref. [11] adopted the expression shown in Eq. (19), and Ref. [13] adopted the expression shown in Eq. (20).

$$Nu = x^*/2 \tag{19}$$

$$\begin{cases} Nu = 2\cdot\dfrac{1-e^{-Nu_s'/\left(0.25x^*\right)}}{Nu_s'/\left(0.25x^*\right)}Nu_s' \\ Nu_s' = 1.89 + \dfrac{0.142\Pr^{1/3}\times\left(0.25x^+\right)^{1.14}}{1+0.211\left(0.25x^+\right)^{0.64}} \end{cases} \tag{20}$$

3) Composite Mode: To facilitate the calculation, Refs. [11] and [13] proposed *Nu* expressions shown as Eqs. (21) and (22) respectively; such expressions can be applied in the developing flow, transition, and fully developed sections.

$$Nu = \left\{\left(\frac{x^*}{2}\right)^{-3} + \left[0.664\sqrt{x^+}\,\Pr^{1/3}\left(1+3.65\Big/\sqrt{x^+}\right)^{1/2}\right]^{-3}\right\}^{-1/3} \tag{21}$$

$$Nu = 2\cdot\frac{1-e^{-1.89/\left(0.25x^*\right)}}{1.89/\left(0.25x^*\right)}\left\{1.89 + \frac{0.142\Pr^{1/3}\left(0.25x^+\right)^{1.14}}{1+0.211\left(0.25x^+\right)^{0.64}}\right\} \tag{22}$$

4) Engineering Expression of Nu: Nu expressions are complex in Eqs. (15)-(22). Therefore, the engineering expression shown in Eq. (23) is introduced by mathematically fitting *Nu* expressions proposed in Refs. [11]-[18]. This expression is suitable for the process from the developing flow section to the fully developed section, and it is concise and easy to calculate.

$$Nu = \left[23.4\left(x^+\right)^{-3} + \left(x^+\right)^{-1.28}\right]^{-1/3} \tag{23}$$

The heat transfer coefficient *h* can be obtained by using Eq. (23), $x^+ = Re \cdot s/L$, and $h = Nuk_a/s$.

To compare the error of Eq. (23), the curves of *Nu* shown in Fig. 9 are drawn according to Eqs. (15)-(18) and Eqs. (21)-(23) of the developing flow section; the curves of *Nu* shown in Fig. 10 are drawn according to Eqs. (19)-(23) of the fully developed section. For comparison, *Pr* is 0.7 when drawing Figs. 9 and 10, and $d = s$ is approximately taken. The curve of Eq. (18) represents only one channel of fins. In Fig. 9, given that the upper limit range of the curve of Eq. (18) is $Re{\cdot}s/L = 125$, no reference value is used when crossing the border [14], [15]. The expressions of the developing flow section shown in Eqs. (15)-(18) are valid only when it takes approximately $Re{\cdot}s/L > 20$. The expressions of the fully developed section shown in Eqs. (19) and (20) are valid only when they utilize approximately $Re{\cdot}s/L < 3$.

As shown in Figs. 9 and 10, the curves of Eq. (23) are

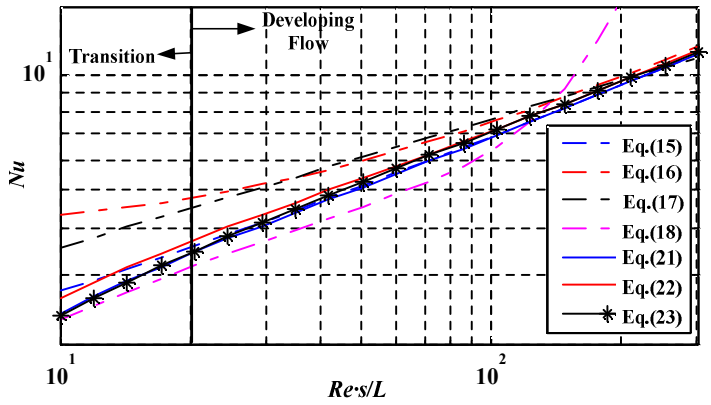

Fig. 9. *Nu* of the developing flow section.

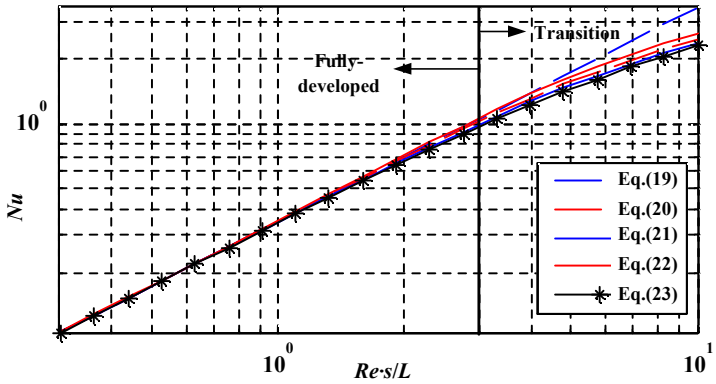

Fig. 10. *Nu* of the fully developed section.

located among the curves of Eqs. (15)-(18), (21), and (22) in the developing flow section, that is, when $Re{\cdot}s/L > 20$. The curve of Eq. (23) is slightly lower than those of Eqs. (19)-(22) in the fully developed section, that is, when $Re{\cdot}s/L < 3$. The curve of Eq. (23) is insignificantly lower than those of Eqs. (21) and (22) in the transition section, that is, when $3 < Re{\cdot}s/L < 20$.

According to the preceding analysis, the complexity of Eq. (23) is significantly lower than that of existing expressions. Meanwhile, the accuracy is only slightly lower than that of existing expressions.

D. Pressure Drop of Heat Sink

The frictional air pressure drop in a heat sink can directly influence the volumetric flow rate of the fan, which is related to the effect of the air-cooled design. This section investigates the frictional air pressure drop of heat sinks.

Heat sink causes the total pressure drop, as follows:

$$\Delta p_{\mathrm{a}} = \Delta p_{\mathrm{c}} + \Delta p_{\mathrm{l}}, \tag{24}$$

where $\triangle p_{\mathrm{l}}$ represents the sum of the inlet and outlet pressure drop, and $\triangle p_{\mathrm{c}}$ represents the core pressure drop. $\triangle p_{\mathrm{l}}$ is

$$\begin{cases} \Delta p_{\mathrm{l}} = \left(K_{\mathrm{c}} + K_{\mathrm{e}}\right)\rho_{\mathrm{a}} V_{\max}^2 / 2 \\ K_{\mathrm{c}} = 0.8 - 0.4\varepsilon^2 \\ K_{\mathrm{e}} = \left(1-\varepsilon\right)^2 - 0.4\varepsilon \\ \varepsilon = s/\left(s + t_{\mathrm{a}}\right) \end{cases}. \tag{25}$$

Δp_{c} is

$$\Delta p_{\mathrm{c}} = \left[4 f_{\mathrm{app}} \cdot 2Re / \left(4x^{+}\right)\right]\left(\rho_{\mathrm{a}} V_{\mathrm{a}\max}^2 / 2\right). \tag{26}$$

where f_{app} is the apparent friction factor. The calculation of $2f_{\mathrm{app}}Re$ in Refs. [14] and [15] adopted Eq. (27), and Ref. [16] adopted Eq. (28). For high-power cooling fins, $s/H < 1/6$ generally, and Eqs. (27) and (28) are similar. Therefore, Δp_{c} can be calculated with either of the following equations:

$$\begin{aligned} 2 f_{\mathrm{app}} Re = {} & 23.7366 + 0.219847 \times \left(4x^{+}\right) \\ & - 6.43526 \times 10^{-3} \times \left(4x^{+}\right)^{1.5} + 7.39124 \times 10^{-5} \times \left(4x^{+}\right)^{2}, \\ & - 3.81290 \times 10^{-9} \times \left(4x^{+}\right)^{3} \end{aligned} \tag{27}$$

$$\begin{cases} 2 f_{\mathrm{app}} Re = \left[\left(3.44\sqrt{4x^{+}}\right)^2 + \left(2fRe\right)^2\right]^{1/2} \\ 2fRe = 24 - 32.527\left(\dfrac{s}{H}\right) + 46.721\left(\dfrac{s}{H}\right)^2 \\ \qquad - 40.829\left(\dfrac{s}{H}\right)^3 + 22.954\left(\dfrac{s}{H}\right)^4 - 6.089\left(\dfrac{s}{H}\right)^5 \end{cases}, \tag{28}$$

where f is the friction factor.

E. Fan Characteristics

For fans, the relationship between volumetric flow rate and

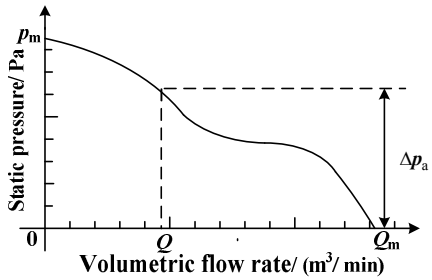

Fig. 11. Relationship between volumetric flow rate and static pressure.

static pressure is shown in Fig. 11 [27]. This figure is generally given in the fan specification. When the total pressure drop of the heat sink is $\triangle p_a$, the corresponding actual volumetric flow rate is shown as Q in Fig. 11. Q_m and p_m in Fig. 11 represent the rated volumetric flow rate and the rated static pressure of the fan respectively.

According to Ref. [28], the following equation is reasonable to some extent:

$$n/n_m = Q/Q_m = \sqrt{p/p_m} = \sqrt[3]{N/N_m}\,, \tag{29}$$

where n, p, and N represent the rotational speed, static pressure, and shaft power of the fan, respectively. The subscript m represents the rated value. Therefore, Eq. (29) and the given parameters in the fan specification can be used to estimate the fan performance.

The relationship between the actual volumetric flow rate Q and the thermal dissipation power P of the fan is shown in Eq. (30). This equation can be used to estimate the volumetric flow rate of the fan. The unit of Q in Eq. (30) is m^3/min, and the other variables use System International units.

$$Q = 60P/\left(\rho_a c_a \Delta T_a\right), \tag{30}$$

where c_a is the specific heat capacity of air with a value of 1000 J/(kg·°C). $\rho_a = 1.20$ kg/m^3 at 20 °C. ΔT_a is the temperature difference between inlet and outlet air. The outlet temperature should not be higher than 71 °C.

When the power is relatively high, a single fan generally cannot provide thermal dissipation. Several fans running together are needed. Fans in series mainly change the air pressure, and fans in parallel mainly change the volumetric flow rate. Therefore, if the total pressure drop of the heat sink is relatively high, the series operation will be efficient. If the volumetric flow rate is insufficient, the parallel operation will be efficient.

For fans with the same size, their volumetric flow rate and air pressure differ [20], and the effect of thermal dissipation has a great difference. Therefore, fans with medium performance should be adopted for an air-cooled design. Replacing medium-performance fans with high-performance fans that have the same size is simple and efficient if the air-cooled design cannot meet the requirements.

F. Air-cooled Design Process

1) Losses should be calculated according to the methods in Section III.B. Different topologies have different switching losses.

Fig. 12. Photo of a 40 kW transmitter.

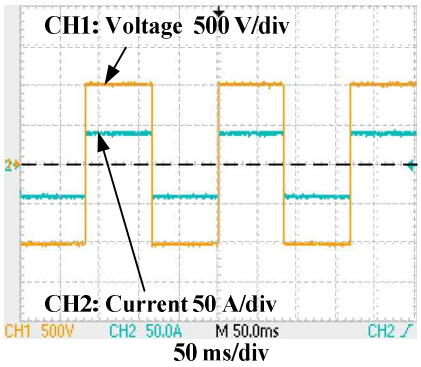

Fig. 13. Output voltage and current waveforms.

2) A heat sink should be selected first. *Nu* should be calculated according to Eq. (23) with an air velocity of 4 m/s, and the heat transfer coefficient h should then be obtained.
3) Fin efficiency should be calculated according to the method in Section IV.B.
4) Thermal resistance should be calculated according to the method in Section IV.A.
5) Pressure drop of the heat sink should be calculated according to the method in Section IV.D.
6) On the basis of the pressure drop of the heat sink and the thermal dissipation power, fans should be chosen according to the method in Section IV.E. Whether the selected air velocity is reasonable should be examined.
7) If the thermal design cannot meet the requirements, whether to replace heat sink, change the air velocity, or make fans in series or in parallel should be considered. The thermal design should be calculated again according to steps 2)–6).
8) Power devices should be appropriately arranged, and the thermal power should be evenly distributed on the heat

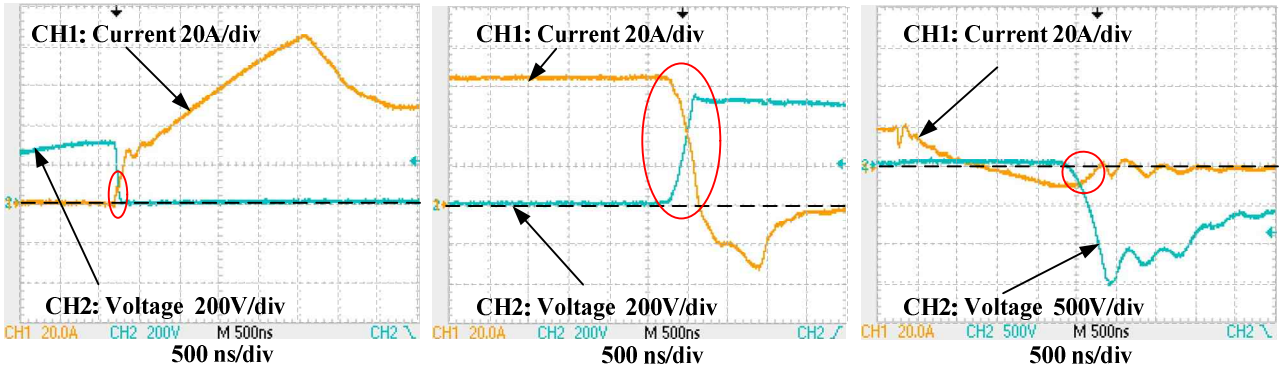

Fig. 14. Transition waveforms in AC–DC power supply. (a) VT_1 turn-on waveforms. (b) VT_1 turn-off waveforms. (c) D_1 reverse recovery waveforms.

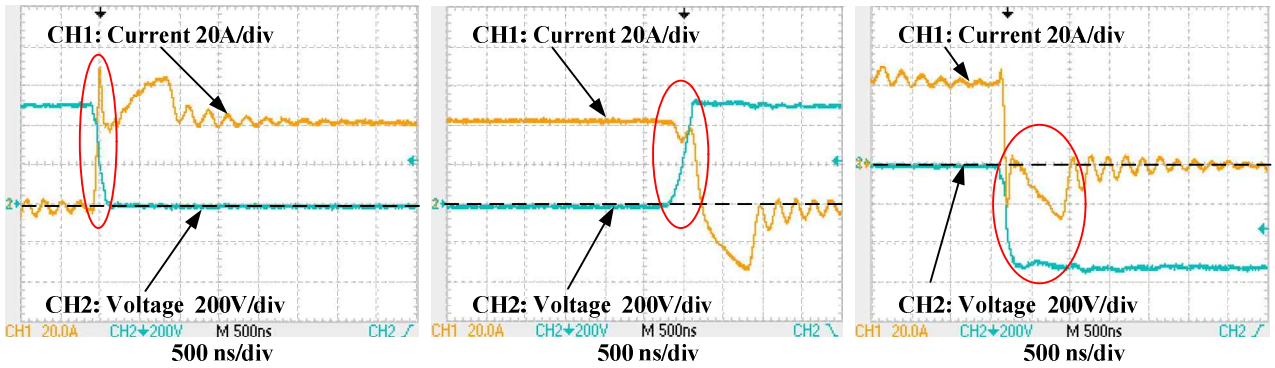

Fig. 15. Transition waveforms in constant-current circuit. (a) VT_2 turn-on waveforms. (b) VT_2 turn-off waveforms. (c) D_2 reverse recovery waveforms.

sink.

9) The air duct should be designed.

V. Measured Results

A. Experimental Conditions

The transmitter runs 8 h a day at 40 kW and operates normally after working for three days. Fig. 12 shows a photo of the working transmitter at 40 kW. Fig. 13 shows the output voltage and current waveforms after thermal stabilization. Fig. 13 shows that the output voltage is more than 1000 V, the current is more than 40 A, and the total output power is more than 40 kW. During the test, waveforms are obtained by using a TDS2012C oscilloscope. The current waveform in Fig. 13 is obtained by using a current probe A622, and the current waveforms in Figs. 14 and 15 are obtained by measuring the voltage on 0.1 Ω resistance. Current values are measured with the oscilloscope. Voltage is obtained by using a UT39A multimeter. Temperature is obtained by using an ST380 infrared thermometer, and the resolution of the infrared thermometer is 1 °C.

B. Transmitter Losses

Fig. 14 shows the turn-on and turn-off waveforms of VT_1, and the reverse recovery waveforms of D_1 in AC–DC power supply. The overlapping area of i_{VT1} and v_{VT1} in Fig. 14(a) is small, that of i_{VT1} and v_{VT1} in Fig. 14(b) is large, and that of i_{D1} and v_{D1} in Fig. 14(c) is small, which are the same as in Fig. 3(a). The overlapping area in Figs. 14(a) and 14(c) are small because the leakage inductance of the transformer in AC–DC power supply limits the change rate of the current. The overlapping area in Fig. 14(b) is large because the current in the leakage inductance of the transformer can only flow through VT_1 before v_{VT1} up to the bus voltage.

Fig. 15 shows the turn-on and turn-off waveforms of VT_2, and the reverse recovery waveforms of D_2 in constant-current circuit. The overlapping areas in Fig. 15(a)-15(c) are large, the same as in Fig. 3(b). The overlapping area in Fig. 15(a) is large because the voltage is clamped to the bus voltage before the current up to the inductance current. The overlapping area in Fig. 15(b) is large because the current is clamped to the inductance current before the voltage up to the bus voltage. Given that the change rate of i_{D2} from 40 A to 0 A is fast, which is determined by the change rate of i_{VT2} from 0 A to 40 A, the overlapping area in Fig. 15(c) is large.

The turn-off loss of VT_1, the turn-on loss and turn-off loss of VT_2, and the reverse recovery loss of D_2 can be calculated using Eq. (1). However, the turn-on loss of VT_1 and the reverse recovery loss of D_1 are only small parts of Eq. (1) and cannot be calculated using the equation. Therefore, when

TABLE V
MEASURED LOSS DATA

	P_1	P_2	P_3
Voltage (V)	490	524	500
Current (A)	43.4	38.0	38.4

TABLE VI
EFFICIENCY OF CALCULATED AND MEASURED VALUES

Efficiency	η_1	η_2	η
Calculated value	94.2%	97.0%	91.4%
Measured value	93.6%	96.4%	90.2%

switching losses are calculated, the circuit topologies should be considered.

The bus voltage and current value after 50 Hz rectifier U_1 are measured to approximately calculate the input power of the AC–DC power supply, which is represented as P_1 in Table V. The output voltage and current of the AC–DC power supply are measured to approximately calculate the output power of the AC–DC power supply, which is represented as P_2. P_2 also represents the input power of the constant-current circuit. The bus voltage and current values between short-circuit protection circuit Z_1 and output full-bridge Z_2 are measured to approximately calculate the output power of the constant-current circuit, which is represented as P_3. The test results are shown in Tables V and VI. To compare the error of loss calculation, the calculated value of the efficiency of the AC–DC power supply, represented as η_1, in Table VI excludes the losses of 50 Hz rectifier bridge U_1 and the losses of the input contactor U_8. The calculated value of the constant-current circuit efficiency, represented as η_2, excludes the losses of the output full-bridge Z_2 and its RC snubber Z_{2R} from Table IV. The efficiency of the transmitter, represented as η, is determined by the product of η_1 and η_2.

The results in Table VI show that the deviation between calculated value of the transmitter and measured value is 1.2%; the calculation deviation of losses is $1.2/(100 - 90.2) \times 100\% = 12.2\%$. The error is reasonable. The proposed thermal loss calculation method in this study is effective and feasible.

C. Temperature Rise of Heat Sink

According to this analysis, a heat sink, SRX-YTJ, with striped rectangular fins is adopted as the heat sink of the AC–DC power supply with parameters of $s = 4.8$ mm, $t_a = 2.5$ mm, $t_b = 13$ mm, $c_1 = 2$, $H = 62$ mm, $L = 350$ mm, $W = 360$ mm, $n_f = 49$, and $k_f = 160$ W/(m·°C). Three parallel fans are adopted for thermal dissipation. The fan model is FFC1212DE, which has the parameters $Q_m = 5.38$ m^3/min, $p_m = 170$ Pa, and $N_m = 29$ W. The temperature of the five test points are measured on the heat sink of the AC–DC power supply shown in Fig. 16, and the results are shown in Table VII. The representation of the devices U_1, U_2, U_{2R}, U_4, U_{4R}, and U_6 is indicated in Table III. The ambient temperature is 21 °C. Table VII shows that the average temperature rise is 22 °C, the temperatures of the five points are relatively even, and the design of the thermal dissipation is reasonable.

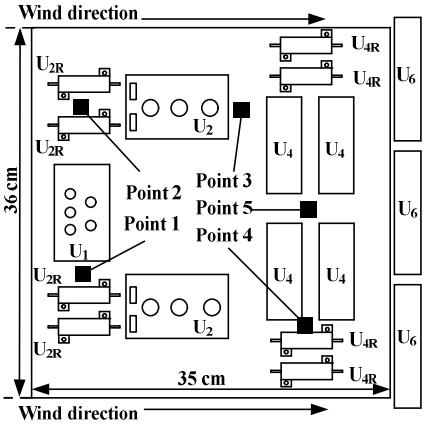

Fig. 16. Distribution of measured points.

TABLE VII
TEMPERATURE OF THE HEAT SINK

Point	1	2	3	4	5
Temperature (°C)	37	57	44	37	38

VI. CONCLUSIONS

1) The rated voltage of IGBTs in the cascaded transmitter can be half of that in the integrated transmitter for adopting cascaded topology, which can reduce the switching losses of the transmitter. If the AC–DC power supply adopts constant-current control in future research, the constant current circuit in this study can be deleted and the transmitter losses reduced.
2) The full-bridge inverter IGBTs in the AC–DC power supply and the chopper switch IGBT in the constant-current circuit have different voltage and current transition waveforms. The high-frequency rectifier diodes in the AC–DC power supply and chopper diode in the constant-current circuit also have different reverse recovery voltage and current waveforms. The switching losses of the power devices should be calculated according to the topologies.
3) Striped fins mainly change the surface area of thermal dissipation. The thermal resistance of a heat sink with striped fins can be calculated by multiplying the heat transfer coefficient by a striped coefficient under the smooth fin model, and the striped coefficient can be calculated by dividing the total surface area of striped fins by the total surface area of the corresponding smooth fins. The heat sink can cause a frictional air pressure drop, while the volumetric flow rate of the fan decreases with the increase in pressure drop. Therefore, the effect of pressure drop of the heat sink should be

considered. Medium-performance fans should be adopted for an air-cooled design. Replacing medium-performance fans with high-performance fans that have the same size is simple and efficient if the air-cooled design cannot meet the requirements.

4) The measured results show that the deviation between calculated value and measured value of the transmitter losses is 12.2%, which meets the error design requirements of less than 25%. The temperature of each point on the heat sink of AC–DC power supply is roughly even, and the average temperature of the heat sink is 22 °C, which meets the design requirements of the temperature rise between 20 °C and 40 °C. The transmitter has favorable thermal stability with an output power of 40 kW.
5) To some extent, the proposed air-cooled design can be used in other power electronic equipment below 100 kW.

REFERENCES

[1] Z. G. An, Q. Y. Di, C. M. Fu, C. Xu, and B. Cheng, "Geophysical evidence through a CSAMT survey of the deep geological structure at a potential radioactive waste site at Beishan, Gansu, China," *J. Environ. Eng. Geophys.*, Vol. 18, No. 1, pp. 43-54, Mar. 2013.

[2] G. J. Wu, X. Y. Hu, G. P. Huo, and X. C. Zhou, "Geophysical exploration for geothermal resources: an application of MT and CSAMT in Jiangxia, Wuhan, China," *J. Earth Sci.*, Vol. 23, No. 5, pp. 757-767, Oct. 2012.

[3] S. B. Singh, G. A. Babu, B. Veeraiah, and O. P. Pandey, "Thinning of granitic-gneissic crust below uplifting Hyderabad granitic region of the eastern Dharwar Craton (South Indian Shield): evidence from AMT/CSAMT experiment," *J. Geol. Soc. India*, Vol. 74, No. 6, pp. 697-702, Dec. 2009.

[4] F. Yu and Y. M. Zhang, "Modeling and control method for high-power electromagnetic transmitter power supplies," *Journal of Power Electronics*, Vol. 13, No. 4, pp. 679-691, Jul. 2013.

[5] Q. Y. Jiang, "Study on the key technology of wide field electromagnetic sounding instrument," Ph.D. Thesis, Central South University, Changsha, China, 2010.

[6] Q. H. Zhen, Q. Y. Di, and H. B. Liu, "Key technology study on CSAMT transmitter with excitation control," *Chinese J. Geophys.,* Vol. 56, No. 11, pp. 3751- 3760, Nov. 2013.

[7] F. S. Shi, "A study on high power multi-function transmitting system," *Progress in Geophysics*, Vol. 24, No. 3, pp. 1109-1114, Jun. 2009.

[8] P. R. Lin, P. Guo, F. S. Shi, C. J. Zheng, Y. Li, J. H. Li, and B. L. Xu, ''A study of the techniques for large-depth and multi-functional electromagnetic survey," *Acta Geoscientica Sinica*, Vol. 31, No. 2, pp. 149-154, Apr. 2010.

[9] Z. Y. Zhang, G. Q. Xu, and X. L. Shen, "Analyzing and designing of dissipation system of inverter," *Journal of Tongji University (Natural Science)*, Vol. 32, No. 6, pp. 775-778, Jun. 2004.

[10] W. Z. He, D. Y. Qiu, W. X. Xiao, and B. Zhang, "Thermal design of high frequency high power switched-mode power supply," *Trans. China Electrotechnical Society*, Vol. 28, No. 2, pp. 185-191,218, Feb. 2013.

[11] P. Teertstra, M. M. Yovanovich, and J. R. Culham, "Analytical forced convection modeling of plate fin heat sinks, " *Journal of Electronics Manufacturing*, Vol. 10, No. 4, pp. 253-261, Dec. 2000.

[12] T. Y. Kim and S. J. Kim, "Fluid flow and heat transfer characteristics of cross-cut heat sinks," *Int. J. Heat Mass Transfer*, Vol. 52, No. 23-24, pp. 5358-5370, Nov. 2009.

[13] Y. Sata, H. Iwasaki, and M. Ishizuka, "Development of prediction technique for cooling performance of finned heat sink in uniform flow," *IEEE Trans. Compon. Packag. Manuf. Technol. Part A*, Vol. 20, No. 2, pp. 160-166, Jun. 1997.

[14] S. Y. Kim and R. L. Webb, "Analysis of convective thermal resistance in ducted fan-heat sinks," *IEEE Trans. Compon. Packag. Technol.*, Vol. 29, No. 3, pp. 439-448, Sep. 2006.

[15] S. W. Karng, J. H. Shin, H. S. Han, Y. H. Kim, and S. Y. Kim, "Thermal performance of a thermoelectric air-cooling system with heat sinks," in *ITHERM*, pp. 1-7, 2010.

[16] S. J. Kim, D. K. Kim, and H. H. Oh, "Comparison of fluid flow and thermal characteristics of plate-fin and pin-fin heat sinks subject to a parallel flow," *Heat Transfer Eng.*, Vol. 29, No. 2, pp. 169-177, Feb. 2008.

[17] Z. P. Duan and Y. S. Muzychka, "Experimental investigation of heat transfer in impingement air cooled plate fin heat sinks," *J. Electron. Packag.*, Vol. 128, No. 4, pp. 412-418, Dec. 2006.

[18] G. S. Dai, *Heat Transfer,* 2nd ed., Higher Education Press, Beijing, pp. 37-46, 255-258, 2011.

[19] J. Deans, J. Neale, W. Dempster, and C. K. Lee, "The use of effectiveness concepts to calculate the thermal resistance of parallel plate heat sinks," *Heat Transfer Eng.*, Vol. 27, No. 5, pp. 56-67, Jun. 2006.

[20] DC Brushless Fans & Blowers, http: //www.delta.com.tw /product /cp /dcfans /dcfans_main.asp, Oct. 5th 2014.

[21] D. W. Xu, H. W. Lu, L. P. Huang, S. Azuma, M. Kimata, and R. Uchida, "Power loss and junction temperature analysis of power semiconductor devices," *IEEE Trans. Ind. Appl.*, Vol. 38, No. 8, pp. 1426-1431, Sep/Oct. 2002.

[22] K. Takao, and H. Ohashi, "Accurate power circuit loss estimation method for power converters with Si-IGBT and SiC-diode hybrid pair," *IEEE Trans. Electron. Devices*, Vol. 60, No. 2, pp. 606-612, Feb. 2013.

[23] A. Bhalla, J. Gladish, and G. Dolny, "Effect of IGBT switching dynamics on loss calculations in high speed applications," *IEEE Electron Device Lett.*, Vol. 20, No. 1, pp. 51-53, Jan. 1999.

[24] K. Mylsamy, R. Vairamani, G. C. R. Irudayaraj, and H. T. R. Lawrence,"Experimental validation of a cascaded single phase H-bridge inverter with a simplified switching algorithm," *Journal of Power Electronics*, Vol. 14, No. 3, pp. 507-518, May 2014.

[25] W. A. Halim, N. A. Rahim, and M. Azri, "Selective harmonic elimination for a single-phase 13-level TCHB based cascaded multilevel inverter using FPGA," *Journal of Power Electronics*, Vol. 14, No. 3, pp. 488-498, May 2014.

[26] J. P. Lee, B. D. Min, and D. W. Yoo, "Implementation of a high efficiency grid-tied multi-level photovoltaic power

conditioning system using phase shifted H-bridge modules," *Journal of Power Electronics*, Vol. 13, No. 2, pp. 296-303, Mar. 2013.
[27] M. F. Holahan, "Fins, fans, and form: volumetric limits to air-side heatsink performance," *IEEE Trans. Compon. Packag. Technol.*, Vol. 28, No. 2, pp. 255-262, Jun. 2005.
[28] Y. B. Wu, M. S. Zhu, *Engineering Fluid Mechanics Pump and Fan*, Chemical Industry Press, Beijing, pp. 273-275, 2010.

Kai-chang Xue was born in Yunnan, China in 1989. He received his B.S. in Electrical Engineering from Jilin University, Changchun, China in 2010. Currently, he is working toward his Ph.D. at the College of Instrumentation and Electrical Engineering, Jilin University, Changchun, China. His research area is impulse power supply of geophysic instrumentation.

Shuang Wang was born in Jilin, China in 1989. She received her B.S. in Electrical Engineering from Jilin University, Changchun, China in 2013. She is currently working toward her M.S. at the College of Instrumentation and Electrical Engineering, Jilin University, Changchun, China. Her research areas are power electronic technology and application.

Jun Lin was born in Jilin, China in 1954. He received his B.S. and M.S. in Applied Geophysics from Changchun Geological Institute in 1982 and 1987 respectively. He is a professor and a Ph.D. supervisor at the College of Instrumentation and Electrical Engineering, Jilin University, Changchun, China. His research areas are geo-exploration technology and instrumentation, which include seismic instruments, electromagnetic instruments, and nuclear magnetic resonance instruments.

Gang Li was born in Hubei, China, in 1981. He received his B.S. and M.S. in Control Engineering from Central South University, Changsha, China in 2002 and 2005 respectively. He received his Ph.D. in Electrical Engineering from Tsinghua University, Beijing, China in 2009. He is currently a lecturer at the College of Instrumentation and Electrical Engineering, Jilin University, Changchun, China. His research interests include high-power converters, electrical machine drives, and explosion-proof inverters.

Feng-dao Zhou was born in Anhui, China in 1970. He received his B.S. in Electronic Measurement Technology and Instruments from Changchun Geological Institute in 1994, his M.S. in Instrument Science and Technology from Changchun University of Science and Technology in 1999, and his Ph.D. in Instrument Science and Technology from Jilin University in 2010. He is a Professor at the College of Instrumentation and Electrical Engineering, Jilin University, Changchun, China. His research areas are power electronic technology and application in land and marine electromagnetic prospecting instruments.